Journal of Computational Physics **176,** 363–383 (2002)
doi:10.1006/jcph.2002.6992, available online at http://www.idealibrary.com on IDEAL®

A Pressure-Based Method for Turbulent Cavitating Flow Computations

Inanc Senocak and Wei Shyy*

Department of Aerospace Engineering, Mechanics and Engineering Science, University of Florida, Gainesville, Florida 32611
E-mail: *wss@aero.ufl.edu

Received April 18, 2001; revised October 15, 2001

A pressure-based algorithm is presented for turbulent cavitating flow computations. Single-fluid Navier–Stokes equations cast in their conservative form, along with a volume fraction transport equation, are employed. The flow field is computed in both phases with the vapor pressure recovered inside the cavity via a mass transfer model. A pressure–velocity–density coupling scheme is developed to handle the large density ratio associated with cavitation. While no temperature, and hence Mach number, effect is considered in the cavitation model, the resulting pressure–correction equation shares common features with that of high-speed flows, exhibiting a convective–diffusive type, instead of only a diffusive type. Furthermore, similar to high-speed cases, upwinded density interpolation in mass flux computations also aids convergence of the cavitating flow computations. The nonequilibrium effect in the context of the k-ε turbulence model, the grid distribution, and the choice of convection schemes have been computationally examined in projectile flows. While satisfactory predictions in wall pressure distribution can be made with variations in grid resolution and parameters in the cavitation model, other aspects, such as the density distribution and detailed streamline characteristics, are found to exhibit higher sensitivity to them.

NOMENCLATURE

Symbols

b	local characteristic speed
C	arbitrary constant
$C_{\varepsilon 1}, C_{\varepsilon 2}, C_\mu$	turbulence model constants
C_{dest}	empirical constant in the evaporation term
C_P	pressure coefficient
C_{prod}	empirical constant in the condensation term
f	flux at a cell face

0021-9991/02 $35.00

F	flow rate at a cell face
k	turbulent kinetic energy
$\dot{m}^-$	evaporation rate
$\dot{m}^+$	condensation rate
$\vec{n}$	unit normal vector at a cell face
$\vec{u}$	velocity vector
u_i'	fluctuating velocity components in Cartesian coordinates
P	pressure, turbulence production in Eqs. (6)–(7).
P'	pressure correction
q	source term per unit volume
Q	dissipation function
S	surface area of the cell face
U_∞	u-velocity at a reference point
V	volume of the cell
t, t_∞	time, mean flow time scale
α	volume fraction
δ	numerical viscosity parameter
δ_{ij}	Kronecker delta function
ε	turbulent dissipation rate
ϕ	generalized dependent variable
Γ	diffusion coefficient
μ	laminar viscosity
μ_{t}	turbulent viscosity
$\psi(\mathrm{r})$	Minmod flux limiter
τ, τ_{ij}	Reynolds stress tensor
ν_t	kinematic viscosity
ρ_{m}	mixture density
ρ'	density correction
σ	cavitation parameter
σ_{k}, σ_ε	turbulence model constants

Subscripts and Superscripts

cf	cell face
conv	convection
diff	diffusion
i	grid index location in Eqs. (11), (13)–(16), (25), (26)
l	liquid phase
n	iteration level in Eqs. (9)–(12)
p	cell center location
v	vapor phase
∞	freestream
$*$	predicted value

1. INTRODUCTION

In liquid flows, cavitation generally occurs if the pressure drops below the vapor pressure and consequently the negative pressures are relieved by means of forming gas-filled or

gas- and vapor-filled cavities [1]. Cavitation can be observed in a wide variety of hydrodynamic systems, such as pumps, nozzles, injectors, marine propellers, hydrofoils, and underwater bodies [2]. Cavitating flows in most engineering systems are turbulent, and the dynamics of the interface formed involves complex interactions between vapor and liquid phases. These interactions are not well understood in the closure region of the cavity where a distinct interface may not exist and the flow is unsteady. Undesirable features of cavitation are structural damage, noise, and power loss. On the other hand, drag reduction can be observed on bodies surrounded fully or partially with a natural or gas-ventilated cavity [3].

Computational modeling of cavitation has been pursued for years. Early studies primarily utilize the potential flow theory; they are still widely used in many engineering applications. Studies dealing with cavitation modeling through the computation of the Navier–Stokes (N–S) equations have emerged in the last decade. These studies can be put into two categories, namely, interface tracking methods and homogeneous equilibrium flow models.

In the first category, the cavity region is assumed to have a constant pressure equal to the vapor pressure of the corresponding liquid, and the computations are done only for the liquid phase. Constant pressure assumption is physically sensible and has been verified experimentally [4, 5]. Computationally, the liquid–vapor interface can be tracked based on this assumption, along with a wake model to handle the shape of the cavity. Grid is often regenerated iteratively to conform to the cavity shape. These models are capable of simulating sheet cavitation but may not be adequate for cases in which bubble growth and detachment exists. In addition, so far, they are limited to 2-D planar or axisymmetric flows because of the difficulties involved in tracking 3-D interfaces. Examples can be found in Chen and Heister [6] and Deshpande *et al.* [7].

The second category can be termed the homogeneous equilibrium flow models in which the single-fluid modeling approach is employed for both phases. Differences between the various models in this category mostly come from the relation that defines the variable density field. Delannoy and Kueny [8] utilize an arbitrary barotropic equation of state to compute the density field. Likewise, Chen and Heister [9] derive a time- and pressure-dependent differential equation for density. Ventikos and Tzabiras [10] introduce the water-vapor state laws to model the cavitation dynamics, and consider the whole domain, including both vapor and liquid phases, as a compressible fluid. A pressure-based algorithm is adopted, where the density correction in vapor phase is linked to the mass residual there. The results obtained do not seem to recover the cavity vapor pressure in accordance with the cavitation number. Edwards *et al.* [11] use the Sanchez–Lacombe equation of state and solve the temperature transport equation in addition to the Navier–Stokes equations. Considering the isothermal character of cavitating flows in many applications, utilizing a temperature or enthalpy equation and assuming the whole flowfield as compressible may not be the most effective approach. Kubota *et al.* [12] couple the Rayleigh–Plesset equation [13, 14] to the flow solver and compute the void fraction based on the bubble radius. Then the density is calculated using the void fraction formalism. Due to the time-dependent nature of the Rayleigh–Plesset equation, the model is restricted to unsteady cloud cavitation. The authors have also reported that this method is prone to instability because of high-pressure–density dependence, and could not reach the convergence levels of noncavitating flow simulations.

To account for the cavitation dynamics in a more flexible manner, a transport equation model has been recently developed. In this approach, volume or mass fraction of liquid (and

vapor) phase is convected. Singhal *et al*. [15], Merkle *et al*. [16], and Kunz *et al*. [17, 18] have employed similar models based on this concept with differences in the source terms. One apparent advantage of this model comes from the convective character of the equation, which allows modeling of the impact of inertial forces on cavities such as elongation, detachment, and drift of bubbles. Singhal *et al*. [15] utilize a pressure-based algorithm but offer no detailed information related to computational convergence and stability. Merkle *et al*. [16] and Kunz *et al*. [17, 18] have employed the artificial compressibility method with special attention given to the preconditioning formulation. Ahuja *et al*. [19] have developed an algorithm to account for the compressibility effects in the context of artificial compressibility methods with adaptive unstructured grids. Venkateswaran *et al*. [20] have compared the above-mentioned studies, and concluded that all three preconditioning formulations are essentially the same with minor differences.

So far, in the open literature, there seems to be a lack of detailed account of extending pressure-based methods for computing cavitating flows. By pressure-based method, we mean that the pressure field is solved by combining the momentum and mass continuity equations to form a pressure or pressure–correction equation [21–23]. In the present study, a pressure-based algorithm, with conservative formulation, multiblock, and curvilinear grid systems, is adopted to compute cavitating flows. In particular, the coupling between velocity, pressure, and density for proper formulation of the pressure–correction equation for cavitating flow conditions will be discussed. The mass transport equation cavitation model, such as that employed by Kunz *et al*. [17, 18], will be adopted. Although the model considered does not explicitly account for the temperature effect (and hence Mach number effect), it will be demonstrated that the density variations, which are caused by cavitation modeling in the present algorithm, share similar features to that of high-speed flows. This aspect is distinctly different from, say, a low-speed chemically reacting flow [24], where the density variation, while substantial, does not impact the characteristics of the pressure–correction equation. In the low Mach number chemical reacting flows, the pressure–correction equation is of a diffusive type, while in the present cavitating flow model, it is of a convective–diffusive type.

During our literature review, we noticed that criteria to assess computational studies dealing with cavitation, through employment of N–S equations, have not been established yet. Based on our experience, we suggest that a robust computational method must at least satisfy the following conditions:

- The normalized pressure inside the cavity should be equal, or be very close, to the negative value of corresponding cavitation number.
- Density profiles should be plotted to demonstrate that the method handles density ratios on the order of 100–1000 with good convergence levels.
- There should be no spikes or overshoots in pressure profiles from large density jumps across the interface.

In what follows, we first present the governing equations and stable main features of the cavitation model, and then propose numerical schemes that ensure numerical computations. The results to be presented include simulations of both noncavitating and cavitating flows around axisymmetric cylindrical geometries. Also, we investigate the robustness of the numerical framework and the cavitation model through studies of grid refinement, convection schemes, and turbulence modeling.

2. GOVERNING EQUATIONS

The set of governing equations consists of the conservative form of the Reynolds averaged Navier–Stokes equations, plus a volume fraction transport equation to account for the cavitation dynamics. The equations, written in the Cartesian coordinates for the ease of presentation, are presented as follows:

$$\frac{\partial \rho_m}{\partial t} + \nabla \cdot (\rho_m \vec{u}) = 0 \tag{1}$$

$$\frac{\partial}{\partial t}(\rho_m \vec{u}) + \nabla \cdot (\rho_m \vec{u}\vec{u}) = -\nabla P + \nabla \cdot [(\mu + \mu_t)\nabla \vec{u}] + \frac{1}{3}\nabla[(\mu + \mu_t)\nabla \cdot \vec{u}] \tag{2}$$

$$\frac{\partial \alpha_l}{\partial t} + \nabla \cdot (\alpha_l \vec{u}) = (\dot{m}^- + \dot{m}^+). \tag{3}$$

The mixture density and the turbulent viscosity are defined, respectively, as follows:

$$\rho_m = \rho_l \alpha_l + \rho_v (1 - \alpha_l) \quad \mu_t = \frac{\rho_m C_\mu k^2}{\varepsilon}. \tag{4}$$

2.1. Cavitation Modeling

Physically, the cavitation process is governed by the thermodynamics and the kinetics of the phase change dynamics occurring in the system. This complex phenomenon is modeled through $\dot{m}^-$ and $\dot{m}^+$ terms in Eq. (3), which represent evaporation and condensation of the phases, respectively, and results in a variable density field. Surface tension and buoyancy effects are neglected considering the typical situation that Weber and Froude numbers are large. The particular form of these phase transformation rates are adopted from Kunz *et al.* [17, 18]. The values of the empirical constants C_{dest} and C_{prod} for each simulation are presented along with corresponding figures and are different than the values reported in other studies using the same cavitation model. The sensitivity of the simulations to these constants is also studied. The source terms adopted in this study are given below:

$$\dot{m}^- = \frac{C_{\text{dest}} \rho_v \alpha_l MIN[0,\, p - p_v]}{\rho_l \left(\frac{1}{2}\rho_l U_\infty^2\right) t_\infty} \quad \dot{m}^+ = \frac{C_{\text{prod}} \rho_v \alpha_l^2 (1 - \alpha_l)}{\rho_l t_\infty}. \tag{5}$$

The time scale in the equation is defined as the ratio of the characteristic length scale to the reference velocity scale (l/U). The nominal density ratio (ρ_l/ρ_v) is the ratio between thermodynamic values of density of liquid and vapor phases at the corresponding flow condition; a value of 1000 is taken for this ratio in all computations in this study.

2.2. Turbulence Modeling

For the turbulence closure, the original k-ε turbulence model with wall functions is adopted [25]:

$$\frac{\partial \rho_m k}{\partial t} + \nabla \cdot (\rho_m k \vec{u}) = (\boldsymbol{\tau} \cdot \nabla k) \cdot \vec{u} - \rho_m \varepsilon + \nabla \cdot \left(\left(\mu + \frac{\mu_t}{\sigma_k} \right) \nabla k \right) \tag{6}$$

$$\frac{\partial \rho_m \varepsilon}{\partial t} + \nabla \cdot (\rho_m \varepsilon \vec{u}) = C_{\varepsilon 1} \frac{\varepsilon}{k} P - C_{\varepsilon 2} \rho_m \frac{\varepsilon^2}{k} + \nabla \cdot \left(\left(\mu + \frac{\mu_t}{\sigma_\varepsilon} \right) \nabla \varepsilon \right). \tag{7}$$

TABLE I
Empirical Constants Used in k-ε Turbulence Model

MODEL	C_μ	$C_{\varepsilon 1}$	$C_{\varepsilon 2}$	σ_k	σ_ε
Original k-ε	0.09	1.44	1.92	1.0	1.3
Nonequilibrium k-ε	0.09	$1.15 + 0.25(\mathrm{P}/\varepsilon)$	$1.45 + 0.45(\mathrm{P}/\varepsilon)$	0.8927	1.15

The turbulent production, Reynolds stress tensor term, and the Boussinesq eddy viscosity concept are defined as follows:

$$P = (\boldsymbol{\tau} \cdot \nabla k) \cdot \vec{u} \quad \boldsymbol{\tau} = \tau_{ij} = -\overline{\rho u_i' u_j'} \quad \overline{u_i' u_j'} = \frac{2}{3} k \delta_{ij} - \nu_t \left(\frac{\partial u_i}{\partial x_j} + \frac{\partial u_j}{\partial x_i} \right). \tag{8}$$

In the above equations $C_{\varepsilon 1}$, $C_{\varepsilon 2}$, σ_k, σ_ε are empirical constants. For certain types of flows, such as flows with recirculation, rotation and large streamline curvatures, equilibrium between the turbulent production and dissipation is not maintained, these constants should be modified because they are originally determined based on the equilibrium conditions. The coefficients $C_{\varepsilon 1}$, $C_{\varepsilon 2}$ regulate the production and dissipation in the ε equation, respectively. Among the variants introduced to modify the empirical constants, we investigate the so-called nonequilibrium k-ε in this study. The empirical constants used in these models are tabulated in Table I. Further information about these models and applications for different test cases is given in Shyy *et al.* [26].

3. NUMERICAL METHODOLOGY

The present Navier–Stokes solver, documented in [23, 26, 27], employs a pressure-based algorithm and a finite volume approach to solve the fluid flow and energy equations, on collocated multiblock grids in 2-D and 3-D domains. For the present cavitation model, Eq. (3), the volume fraction transport equation with appropriate source terms given in Eq. (5), needs to be implemented into the solver. To help describe the underlying algorithm we adopt the steady-state generic transport equation in vector form as

$$\nabla \cdot (\rho \vec{u} \phi) = \nabla \cdot (\Gamma \nabla \phi) + q_\phi, \tag{9}$$

where ϕ is the generalized dependent variable, Γ is the diffusion coefficient, and the second term on the right-hand side represents the source term for the transported quantity ϕ. The above equation is transformed to an integral form, suitable for finite volume discretization, using the divergence theorem,

$$\oint_s (\rho \vec{u} \phi - \Gamma \nabla \phi) \cdot \vec{n} \, dS = \int_v q_\phi \, dV, \tag{10}$$

which upon integration yields the equation

$$F_{i+\frac{1}{2},j} + F_{i-\frac{1}{2},j} + F_{i,j+\frac{1}{2}} + F_{i,j-\frac{1}{2}} = b_i, \tag{11}$$

where b_i is the integrated form of the source term, and F represents the flux of ϕ at each control volume face and is composed of a convective and a diffusive part as follows:

$$F_{\mathrm{cf}} = F_{\mathrm{cf}}^{\mathrm{conv}} + F_{\mathrm{cf}}^{\mathrm{diff}} = (\rho\vec{u}\phi - \Gamma\nabla\phi)\cdot\vec{n}S_{\mathrm{cf}}. \tag{12}$$

The diffusive flux is discretized using the second-order central difference scheme, whereas the choice of discretization scheme for the convective flux often depends on the flow conditions and fluid physics [23]. In this study we consider two schemes, namely, the first-order upwind (FOU) and the second-order controlled variation scheme (CVS) [28, 29]. The first-order upwind scheme is employed mainly to probe the sensitivity of the solution with respect to the choice of the convection operators. The CVS scheme is employed in all cases for experimental validation. Both convection schemes are illustrated considering the one-dimensional transport equation of the variable ϕ. In the first-order upwind (FOU) scheme, the value of the dependent variable is estimated using the upwind neighbor value. If we let $f_{i+1/2}$ be the first-order flux at a control volume face, determined through first-order extrapolations of two immediate neighboring cells, then the scheme can simply be written as

$$f_{i+\frac{1}{2}} = \phi_i^{n+1}\,\mathrm{Max}\left(\rho_{i+\frac{1}{2}}u^n_{i+\frac{1}{2}}, 0\right) - \phi_{i+1}^{n+1}\,\mathrm{Max}\left(-\rho_{i+\frac{1}{2}}u^n_{i+\frac{1}{2}}, 0\right), \tag{13}$$

where u is the velocity component in the corresponding direction.

Higher-order spatial accuracy can be obtained by employing more grid points for extrapolation. However, it is known that second-order-accurate schemes for convection terms produce oscillations around discontinuities. Later, in the results section, it will be shown that shock-like discontinuities in density profiles do appear in cavitating flows. If a linear second-order upwind scheme is used, oscillations in the vicinity of discontinuities can interfere with the mass transfer model and can lead to unrealistic solution or even divergence. For this reason, the numerical methodology must introduce a convection scheme that does not generate nonphysical oscillations in the vicinity of sharp gradients and discontinuities.

The second-order-accurate CVS scheme [28, 29] is based on the total variation-diminishing (TVD) concept [30] and is suitable for the present problem. In the CVS scheme, the convective flux is estimated using the second-order TVD scheme [30] to improve the formal order of accuracy and the local characteristic speeds are assigned according to the value of the local convective speed. The second-order net flux term for the linearized implicit version of the CVS is presented as follows:

$$\begin{aligned} f^{(2)}_{i+\frac{1}{2}} - f^{(2)}_{i-\frac{1}{2}} = {} & \frac{1}{2}\rho_{i+\frac{1}{2}}\left\{\left[b_{i+\frac{1}{2}} - Q_{i+\frac{1}{2}}\right]\left[1 + \frac{1}{2}\psi\left(r^-_{i+\frac{1}{2}}\right)\right]\right\}^n(\phi_{i+1} - \phi_i)^{n+1} \\ & - \frac{1}{2}\rho_{i-\frac{1}{2}}\left\{\left[-b_{i-\frac{1}{2}} - Q_{i-\frac{1}{2}}\right]\left[1 + \frac{1}{2}\psi\left(r^+_{i-\frac{1}{2}}\right)\right]\right\}^n(\phi_i - \phi_{i-1})^{n+1} \\ & + \frac{1}{4}\rho_{i+\frac{3}{2}}\left\{\psi\left(r^-_{i+\frac{3}{2}}\right)\left[-b_{i+\frac{3}{2}} + Q_{i+\frac{3}{2}}\right](\phi_{i+2} - \phi_{i+1})\right\}^n \\ & - \frac{1}{4}\rho_{i-\frac{3}{2}}\left\{\psi\left(r^+_{i-\frac{3}{2}}\right)\left[b_{i-\frac{3}{2}} + Q_{i-\frac{3}{2}}\right](\phi_{i-1} - \phi_{i-2})\right\}^n. \end{aligned} \tag{14}$$

The superscript (2) stands for second-order accuracy, $(n+1)$ represents the value at the current iteration, and subscript (i) indicates the cell center location. The function $\psi(r)$

and Q are the Minmod flux limiter and the dissipation function, respectively, and they are defined as follows:

$$\psi(r) = \max[0, \min(1, r)], \quad r^{+}_{i+\frac{1}{2}} = \frac{f_{i+2} - f_{i+\frac{3}{2}}}{f_{i+1} - f_{i+\frac{1}{2}}}, \quad r^{-}_{i+\frac{1}{2}} = \frac{f_{i-1} - f_{i-\frac{1}{2}}}{f_i - f_{i+\frac{1}{2}}} \tag{15}$$

$$Q_{i+\frac{1}{2}} \equiv Q\left(b_{i+\frac{1}{2}}\right) \begin{cases} \frac{1}{2}\left(\frac{b^2}{\delta} + \delta\right), & \text{if } |b| < \delta \\ |b|, & \text{if } |b| \geq \delta. \end{cases} \tag{16}$$

The parameter δ is used to regulate the numerical viscosity; in this study it is assigned as zero, which results in the clipping of the fluxes. Local characteristic speed b is assigned according to the value of the cell face velocity.

3.1. Pressure-Based Algorithm

The pressure-based algorithm adopted in this study follows the spirit of the well-established SIMPLE algorithm [21], with substantial extension to treat issues associated with curvilinear coordinates and multiblock interface. Basically, the momentum equations are discretized as

$$A^{\vec{u}}_P \vec{u} = \sum A^{\vec{u}}_{nb} \vec{u}_{nb} - V_P (\nabla_d P)_P + b_P, \tag{17}$$

where $A^{\vec{u}}_P$ and $A^{\vec{u}}_{nb}$ are the coefficients of the cell center and neighboring nodes, respectively, due to contributions from convection and diffusion terms. V_P and b_p represent the volume of the cell and the source term, respectively. Note that the ∇_d operator is in the discrete form. The solution procedure is based on the predictor–corrector approach, where the discretized momentum equations is cast as

$$A^{\vec{u}}_P \vec{u}^* = \sum A^{\vec{u}}_{nb} \vec{u}^*_{nb} - V_P (\nabla_d P^*)_P + b_P, \tag{18}$$

indicating that the velocity field at any given location is updated based on the existing values of the neighboring velocity and pressure. Based on Eqs. (17) and (18), velocity corrections can be computed as follows:

$$\vec{u}' = \vec{u} - \vec{u}^* = -\mathbf{D}_P (\nabla_d P')_P \quad \mathbf{D}_P = \begin{bmatrix} V_P/A^u_P & 0 & 0 \\ 0 & V_P/A^v_P & 0 \\ 0 & 0 & V_P/A^w_P \end{bmatrix}. \tag{19}$$

In order to derive corrections for the pressure field, the continuity equation, Eq. (1), is converted to a pressure–correction equation by substituting the corrected velocities:

$$\nabla_d \cdot (\rho \mathbf{D} \nabla_d P') = \nabla_d \cdot (\rho \vec{u}^*). \tag{20}$$

Clearly, the above pressure correction equation has a diffusive nature.

In the pressure-based algorithm, the pressure–correction equation has been revised to achieve successful solutions for highly compressible flows [23, 31, 32]. We will describe this formulation in the context of noncavitating flows with compressibility effects to motivate

the present cavitating flow method. For highly compressible flows, density needs to be corrected to account for the strong pressure–density dependency. For such a formulation the flux terms in the continuity equation will be

$$\rho\vec{u} = (\rho^* + \rho')(\vec{u}^* + \vec{u}') = \rho^*\vec{u}^* + \rho^*\vec{u}' + \rho'\vec{u}^* + \rho'\vec{u}', \tag{21}$$

where $\rho\vec{u}$ term is the mass flux entering the control volume. Starred variables represent the predicted value and primed variables represent the correction terms. The inclusion of the above equation, along with a relation that couples the density to pressure, leads to the following pressure–correction equation:

$$\rho' = C_\rho P' \tag{22}$$

$$-\nabla_d \cdot (\rho^* \mathbf{D} \nabla_d P') + \nabla_d \cdot (C_\rho \vec{u}^* P') = -\nabla_d \cdot (\rho^* \vec{u}^*) + \nabla_d \cdot (C_\rho P' \mathbf{D} \nabla_d P'). \tag{23}$$

By comparing Eqs. (20) and (23), one can see that the characteristics of the pressure–correction equation is altered from a pure diffusive nature to a mixed convective–diffusive nature in regions where density is a function of pressure. As discussed in [23], the relative importance of the first and second terms in Eq. (23) depends on the local Mach number; for low Mach number flows, only the first term prevails, while for high Mach number flows, the second term becomes important. The Mach number dependency can be shown through the equation of state. The fourth term is a nonlinear second-order correction term and it can either be neglected or included in the source term to stabilize the computation in early iterations.

In the cavitation model, a convection equation with pressure-dependent source terms, Eq. (3), is solved to determine the density field. Because of this coupling between pressure and density, the pressure–correction equation needs to be reformulated even though the Mach number effect is not explicitly addressed in the model. Due to Eq. (3) with source terms defined in Eq. (5), once the cavitation model is implemented into a pressure-based algorithm, the pressure–correction equation exhibits a convective–diffusive nature in cavitating regions and purely diffusive nature in the liquid phase. In the present algorithm, the following relation between density correction and pressure correction is introduced to establish the pressure–density coupling,

$$\rho' = C(1 - \alpha_l)P', \tag{24}$$

where C is an arbitrary constant. It should be emphasized that the choice of this constant does not affect the final converged solution because of the nature of the *pressure–correction* equation. Different values of C simply lead to different paths for reaching the converged solution. However, the convective–diffusive nature of the pressure–correction equation is directly affected by the choice. It can easily be shown that the ratio between the convective strength, the second term in Eq. (23), and diffusive strength, the first term in Eq. (23), is directly related to $\mathrm{C}(1 - \alpha_l)$. In the cavity region, the liquid mass fraction decreases, and the pressure–correction equation is of a clear convective–diffusive nature. On the other hand, in the liquid region, the pressure–correction equation returns to a purely diffusive type. Furthermore, it is found that a very large value for C can destabilize the computation in the early stages of the iteration process. For this reason, we suggest $C = \mathrm{O}(1)$ be used. In our computations, $C = 4$ is adopted. It should be noted that the above discussion is based on normalized variables, with the density of the liquid assigned as 1.

The present pressure–velocity–density coupling scheme is along a path responsive to the cavitation dynamics. It is found that the proposed scheme mimics the $\partial\rho/\partial P$ variation

adequately especially near $\alpha = 0$ where the variation is very steep. From the convergence rate point of view, the scheme performs satisfactorily compared to the noncavitating flow computations.

Due to the convective–diffusive nature of the pressure–correction equation for cavitating flows, the coefficient matrix is noticeably asymmetric. Hence, iterative matrix solvers, designed specially for the fast efficient solution of the symmetric problems, need new insight into the precondition treatment. In the present study, we employ the conventional relaxation technique.

Next, we present the practical implementation of the pressure–velocity–density coupling for cavitating flows. For simplicity, we consider the following one-dimensional case to illustrate the nature of the revised pressure–correction equation. Note that a first-order upwind scheme is used for the second term in Eq. (23):

$$a_i P_i' = \left(a_{i+1}^{inc} + C(1-\alpha_l)_{i+1} \max\left[-u_{i+\frac{1}{2}}, 0\right]\right) P_{i+1}' + \left(a_{i-1}^{inc} + C(1-\alpha_l)_{i-1} \max\left[u_{i-\frac{1}{2}}, 0\right]\right) P_{i-1}' + b_i \tag{25}$$

$$a_i = \left(a_{i+1}^{inc} + C(1-\alpha_l)_i \max\left[u_{i+\frac{1}{2}}, 0\right]\right) + \left(a_{i-1}^{inc} + C(1-\alpha_l)_i \max\left[-u_{i-\frac{1}{2}}, 0\right]\right). \tag{26}$$

In this equation, a_{i+1}^{inc} and a_{i-1}^{inc} are the coefficients stemming from an incompressible formulation, b_i is the source term, and α_l is the liquid volume fraction. Subscripts $(i+1)$ and $(i-1)$ stand for the neighboring grid nodes in the east and west directions, respectively. The above form is a combined incompressible–compressible formulation that preserves the incompressible nature in the liquid phase. In the cavitating region, it accounts for the pressure–density dependency in a nonlinear fashion, in accordance with the local value of α_l. This modification is key to a stable computation in which the uniform vapor pressure is recovered in the final converged solution.

Another aspect is that, similar to compressible flow computations, the density at the cell face is upwinded both in the discretized momentum and pressure–correction equations [23, 26, 31]. The criterion for upwinding is based on the value of liquid volume fraction; that is, wherever α_l is less than 1.0, the cell-faced density value is estimated based on an upwinded formula. In regions of sharp density gradients, a single point upwinded extrapolation for density, instead of a two-point interpolation, can significantly improve the convergence level as demonstrated in Fig. 1. The residuals resulting from momentum, mass continuity, and volume fraction transport equations can approach much lower levels than the pressure-based algorithm without an upwinded interpolation for density. It is noted that the residuals are defined as the absolute values of the imbalance of the individual equations summed over the entire number of computational cells, normalized by the total flux of the given variable, at the inlet of the computational domain.

It should also be emphasized that Eq. (24) is not limited to the cavitation model employed in this study; it can easily be adopted for other cavitation models. For example, if an equation of state is utilized to generate the variable density field, then vapor or mass fraction can be derived from density values and used in Eq. (23) to establish the pressure–density coupling.

3.2. Boundary Conditions

Velocity components, volume fractions, and turbulence quantities are specified at the inlet boundary. At the outlet, a zero gradient condition is imposed for pressure correction,

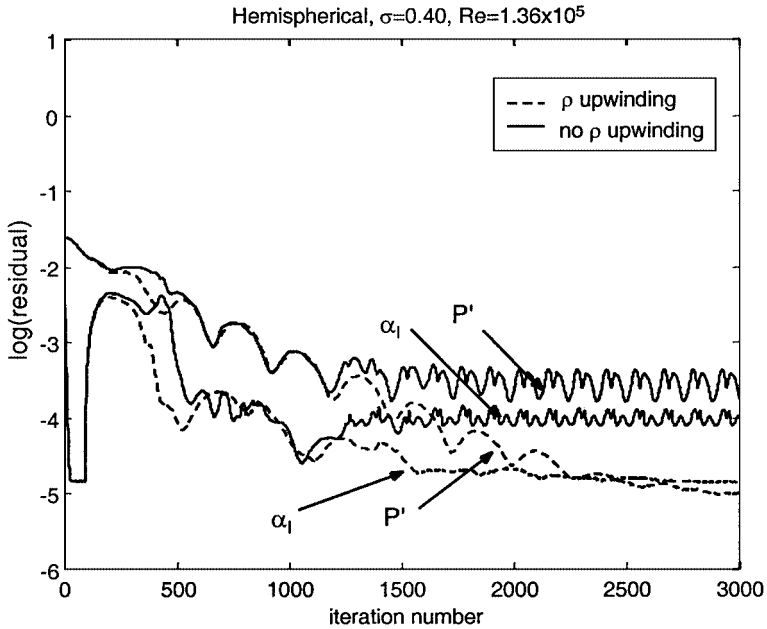

FIG. 1. Improvement in convergence level due to density upwinding. Hemispherical object at $\sigma = 0.40$.

velocity, and volume fraction; in addition, the velocity components are corrected to satisfy the global mass conservation condition with the pressure being fixed at a single upstream node. The pressure value at this node is used to compute the value of vapor pressure for the corresponding cavitation number. At walls, pressure, volume fractions, and turbulence quantities are extrapolated along with no-slip conditions for velocity.

4. RESULTS AND DISCUSSIONS

The formulation presented in the previous section is applied to two different axisymmetric geometries to investigate numerical and physical issues involved in cavitation modeling. Both geometries considered have a cylindrical after-body and they will be referred to according to the shape of their headforms, specifically, hemispherical or blunt. The results include steady-state computations of noncavitating and cavitating flows at a Reynolds number of 1.36×10^5. The cavitation parameter is typically defined as follows:

$$\sigma = \frac{2(P_\infty - P_v)}{\rho U_\infty^2}. \tag{27}$$

Results are compared with experimental results of Rouse and McNown [34] in which pressure coefficients are reported. Since the experimental information does not include time dependency, the steady-state model is adopted in the present computations. From the physical point of view, the steady-state assumption is sensible for sheet cavitation, which has a quasi-steady behavior, with most of the unsteadiness localized in the rear closure region [2, 35, 36]. However, for the blunt object, cavitation may not develop in the form of sheet cavitation. Nevertheless, we have employed the steady-state formulations for both geometries.

We have organized the results into two parts based on the geometry considered. First, we will present the simulations of hemispherical object and discuss issues of grid refinement, convection schemes, and sensitivity to cavitation model parameters. Next, computations of the blunt object will be presented in which we investigate the turbulence modeling issue in the context of the k-ε model. Information related to velocity, pressure, and cavity characteristics will be discussed.

4.1. Simulations of Flow Over a Hemispherical Object

A grid refinement study has been performed to assess the accuracy and sensitivity of the predictions for flows around a hemispherical object. Two grid systems (Grid-A with 119×65 nodes; Grid-B with 231×161 nodes) are generated. Compared to Grid-A, Grid-B has essentially twice the spatial resolution in each direction surrounding the cavity. In both computations, the same modeling parameters given in Fig. 2 are used. Figure 2 shows the pressure coefficient, flow pattern, and density distribution along the body obtained at a cavitation number of 0.40. As can be seen from the plot, the impact of grid resolution on the pressure distribution is not significant. Also, no sharpening of the interface is observed due to grid refinement. However, the density profiles indicate a shorter cavity length for Grid-B. The reason for this shortening is primarily due to the reentrant jet in the rear closure region. By comparing the streamlines and cavity profiles given also in Fig. 2, one can see that the reentrant jet in the closure region is clearer with Grid-B and has a higher strength than with Grid-A. Furthermore, a lower density is observed inside the cavity with Grid-B. It should be emphasized that the pressure profile is not sensitive to the range of grid resolution investigated. Although the flow structure is better resolved with Grid-B, we utilize Grid-A for the rest of the study because of the negligible impact on pressure distribution. This decision is made based on the fact that only pressure distributions are available in the experimental study by Rouse and McNown [34].

Numerical diffusion is a major concern in complex flow computations. In this study, the effect of first- and second-order-accurate convection schemes on solution accuracy is evaluated. In Fig. 3, the pressure coefficient and density profiles, corresponding to a cavitation number of 0.40, are shown. Interestingly, both convection schemes produce

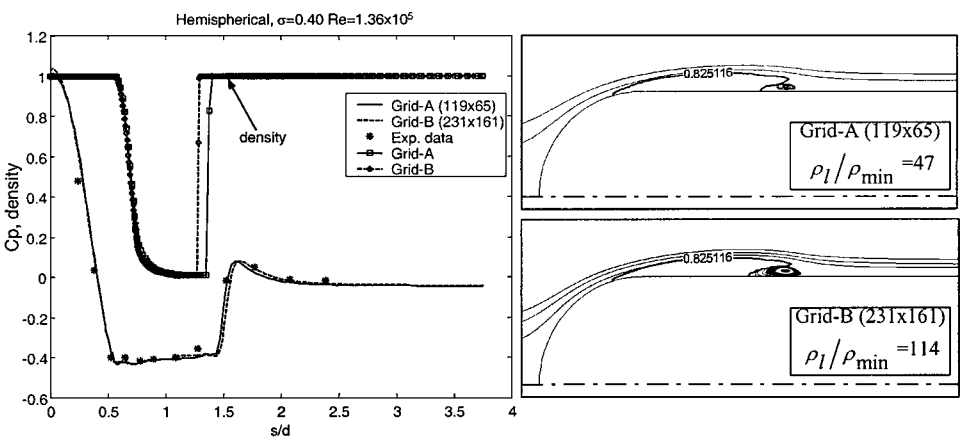

FIG. 2. Grid refinement study for hemispherical object with $\sigma = 0.40$ ($C_{\text{dest}} = 9 \times 10^5$, $C_{\text{prod}} = 3 \times 10^4$, $\rho_l/\rho_v = 1000$). Experimental data are from [34].

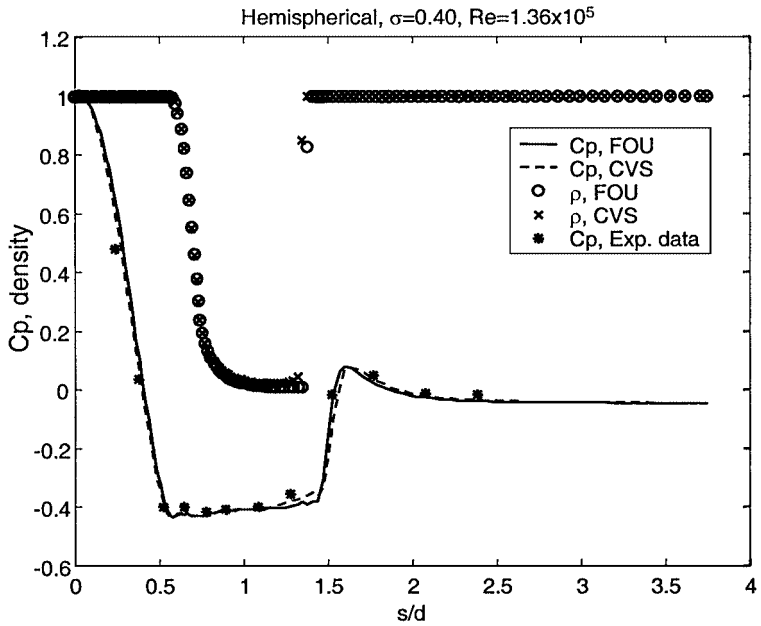

FIG. 3. Effect of convection schemes on pressure coefficient and density distribution for the hemispherical object at $\sigma = 0.40$ ($C_{\text{dest}} = 9 \times 10^5$, $C_{\text{prod}} = 3 \times 10^4$, $\rho_l/\rho_v = 1000$). Grid-A (119×65) is used. Experimental data are from [34].

almost identical results for density and pressure. The density profile is very sharp at the closure region even in the case of first-order upwind scheme (FOU). This phenomenon is mainly an outcome of the cavitation model. Basically the variable density field is generated through source terms for destruction and production of liquid phase. Any smearing is automatically eliminated through activation of the production source term $\dot{m}^+$. As the iteration proceeds, a balance between production and destruction terms is achieved resulting in a cavity profile with uniform pressure and density fields inside. No significant change is observed in flow structure and cavity profiles. Also, the second-order-accurate CVS scheme does not produce any oscillations around the sharp discontinuity at the closure region. Even though the first-order solution appears satisfactory in this case, to ensure that satisfactory results are obtained in other cases, the second-order-accurate CVS scheme is adopted for convection terms throughout the study.

In Fig. 4, the sensitivity of the solutions to model parameters is studied. It can be seen that even increasing these parameters by an order of magnitude has little effect on the pressure coefficient predictions. However, the computed density ratio is noticeably different between these model parameters. Clearly, the computed density ratios can be controlled through adjustment of the model parameters to yield very different solutions while pressure predictions remain unaffected.

Figure 5 demonstrates the predictive capability of the model at cavitation numbers of 0.40 and 0.30 through comparison with experimental data [34]. Identical model parameters are adopted for both cavitation numbers. The pressure distribution corresponding to the noncavitating condition is also plotted for comparison. The present numerical algorithm performs well for both cavitating and noncavitating conditions. The corresponding cavity profiles, streamlines, and computed density ratios are also presented in Fig. 5. The computed

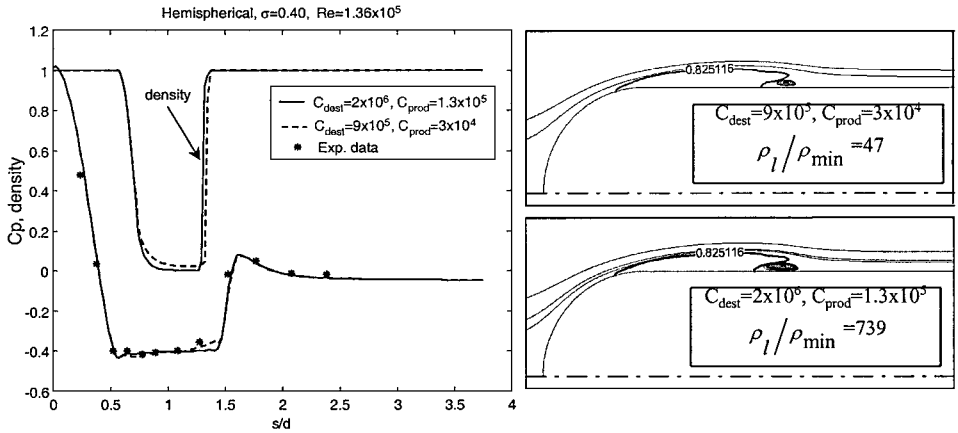

FIG. 4. Sensitivity of modeling parameters for the hemispherical object at $\sigma = 0.40$ ($\rho_l/\rho_v = 1000$). Grid-A (119×65) is used.

cavity profiles are in the form of pinched pockets with reentrant jets in the closure region. With a lower cavitation number ($\sigma = 0.30$), the cavity, as expected, becomes larger than that with a cavitation number ($\sigma = 0.40$). The reentrant jet is also stronger, suggesting that at lower cavitation numbers the reentrant jet can easily perturb the cavity, possibly leading to shedding of bubbles. The computed density ratio is higher for $\sigma = 0.30$ because, similar to what is observed in grid refinement, the source terms are effective on more grid points. The cavity detachment point remains fixed in both of the simulations, which is also in agreement with experimental data.

Gopalan and Katz [36] have recently showed that vorticity production occurs at the closure region of sheet cavities due to baroclinic torque. As shown in Fig. 6, our computations do indicate production of vorticity at the closure region for both cavitation numbers considered, which is consistent with the findings of Gopalan and Katz [36] and, hence, verifies the success of our numerical method. Furthermore, there is no additional production of vorticity at the front part of the cavity indicating that the density and the pressure fields are properly

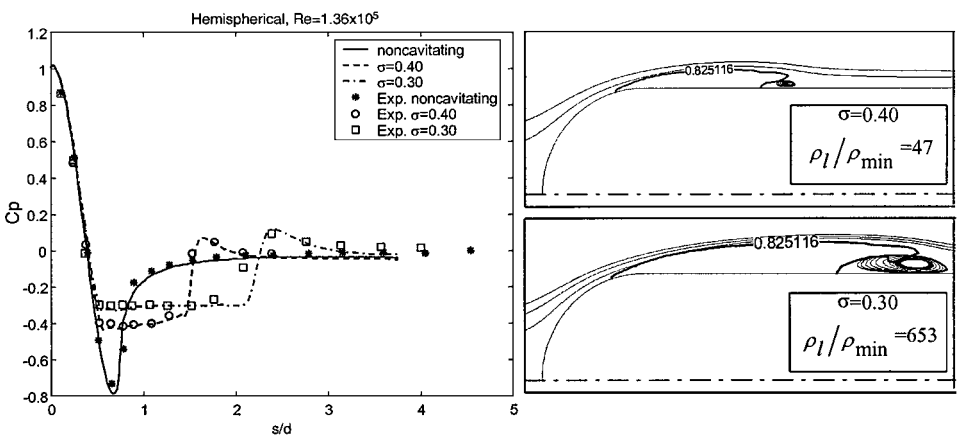

FIG. 5. Comparison of pressure coefficient distributions for hemispherical object under noncavitating and cavitating conditions ($C_{\text{dest}} = 9 \times 10^5$, $C_{\text{prod}} = 3 \times 10^4$, $\rho_l/\rho_v = 1000$). Experimental data are from [34].

FIG. 6. Vorticity generation at the closure region due to baroclinic torque.

computed so that their gradients align parallel to each other without causing any baroclinic vorticity generation.

In Fig. 7, the dynamics of the phase change process is shown. The evaporation process, driven by the pressure difference, is localized at the leading part of the cavity generating the vapor phase. On the other hand, condensation is concentrated along the interface. As a result, these two counteracting processes generate a vapor pocket, which has an almost uniform density (as shown in Fig. 6) and pressure field inside.

4.2. Simulations of Flow Over a Blunt Object

Computations have also been conducted to predict cavitation over blunt cylindrical objects. For this particular object, Rouse and McNown [34] have provided the pressure coefficient distribution along the body, and Katz [37] has reported flow reattachment locations. In view of the potential deficiencies associated with the original k-ε turbulence model [23, 25] for complex flows, a nonequilibrium version of the k-ε model [26], is studied in addition to the original k-ε model. To investigate the turbulence modeling issue, we first consider the noncavitating condition and then extend the study for cavitating conditions. Figure 8 shows the pressure coefficient profile for the noncavitating condition. The original k-ε model fails to match the experimental data in the vicinity of the sharp corner where large strains and streamline curvatures are expected to occur. On the other hand, the nonequilibrium k-ε model performs better to capture the pressure coefficient distribution.

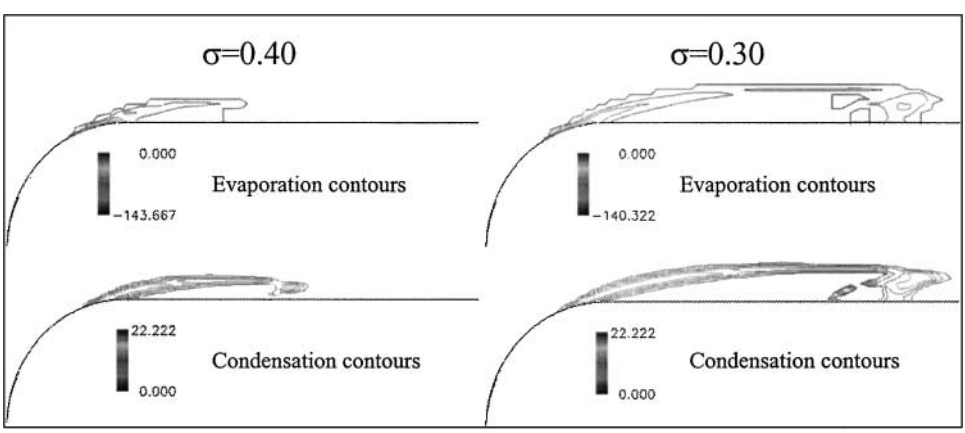

FIG. 7. Dynamics of the phase change.

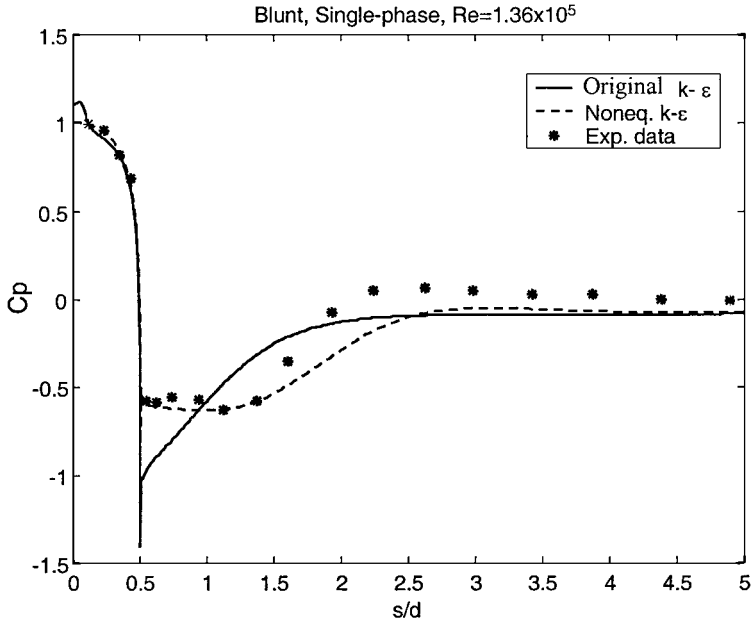

FIG. 8. Impact of turbulence modeling on predictions of pressure coefficient distribution for noncavitating conditions. Experimental data are from [34].

Both models produce comparable solutions far downstream. It should be pointed out that far downstream, pressure distributions are slightly different compared to the experimental data. This is apparently because of the difference between the computational domain and the experimental test section. Figure 9 shows the normalized u-velocity distribution along the

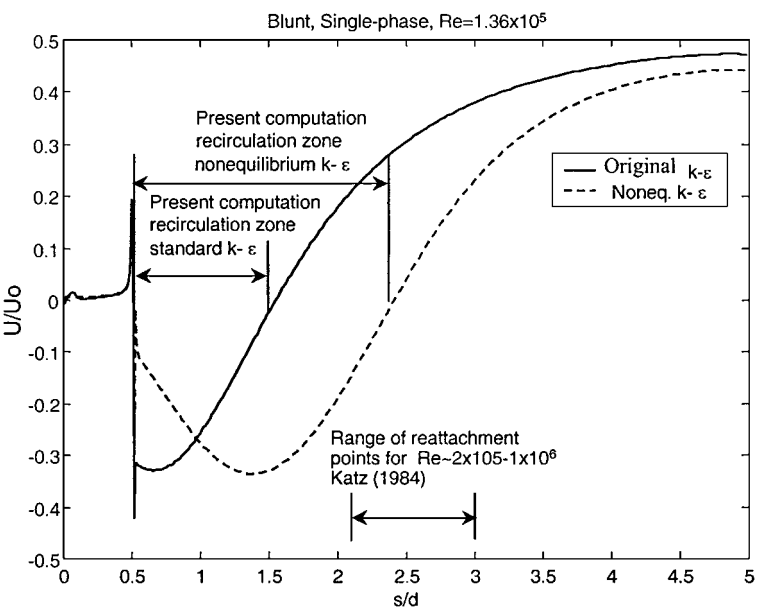

FIG. 9. Effect of turbulence model on separation zones for noncavitating conditions. Experimental data are from [37].

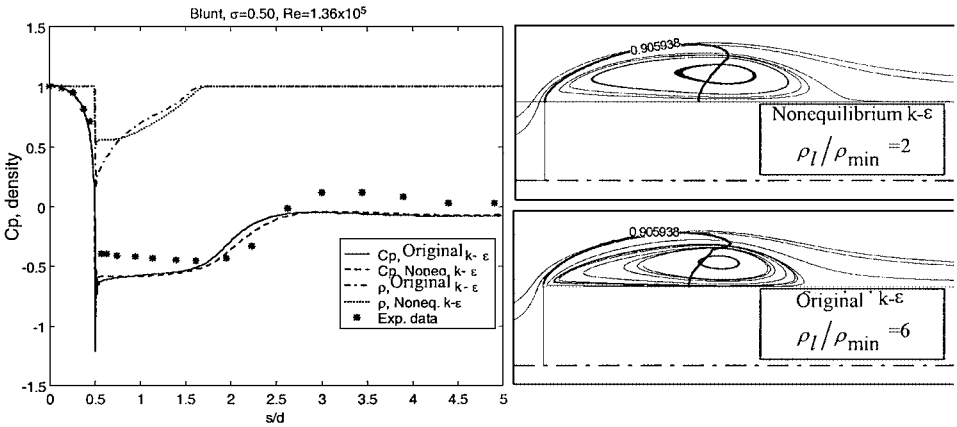

FIG. 10. Impact of turbulence modeling on predictions of pressure coefficient and density distribution ($\sigma = 0.50$, $C_{\text{dest}} = 9 \times 10^3$, $C_{\text{prod}} = 6 \times 10^3$, $\rho_l/\rho_v = 1000$). Experimental data are from [34].

body that is extracted from the first computational nodes away from the solid boundary. The point where velocity changes sign is the reattachment point. One can see that there are considerable differences in predictions of reattachment locations and associated velocity profiles between two turbulence models. It is observed that the reattachment point location, predicted with the nonequilibrium k-ε model, is consistent with the experimental data [37] even though the Reynolds number range is not the same. It should be noted that Katz [37] has not observed a strong correlation between the reattachment location and the Reynolds number for this range. Overall, the nonequilibrium k-ε model performs better, compared to the original k-ε model, in capturing the pressure coefficient distribution and the extent of separation zones. Based on this observation, the nonequilibrium k-ε model is included in the study of cavitating flows over blunt objects.

Figure 10 shows the pressure coefficients and density profiles along the blunt object at a cavitation number of 0.50. Cavity profiles and streamlines are also included in Fig. 8. Computed pressure profiles qualitatively follow the experimentally observed trend. Unlike noncavitating flow computations, both turbulence models considered produce similar results. Figure 11 illustrates the normalized u-velocity profile along the surface. The difference in predicted reattachment location is also less significant between the two turbulence models. Furthermore, both solutions exhibit rather modest density ratios across the cavity interface, suggesting that inside the cavity, the flow exhibits liquid–vapor bubbly structures. In our view, the discrepancy between computational and experimental results may be caused by our steady-state computations. Stinebring *et al.* [38] employ high-speed visualization and report that cavities formed around blunt objects are highly unsteady, and bubbling phenomenon is typically observed. The unsteady computation is expected to offer a better insight for this particular object and will be our focus for future work.

In Fig. 12, the turbulent kinetic energy k and turbulent dissipation rate ε, resulting from the original and nonequilibrium k-ε turbulence models, are compared. In both cases, the turbulent variables are of higher levels following the shear layer surrounding the cavity; however, the detailed distributions are different. The nonequilibrium model yields more substantial presence in both k and ε. Together, they are responsible for a somewhat longer

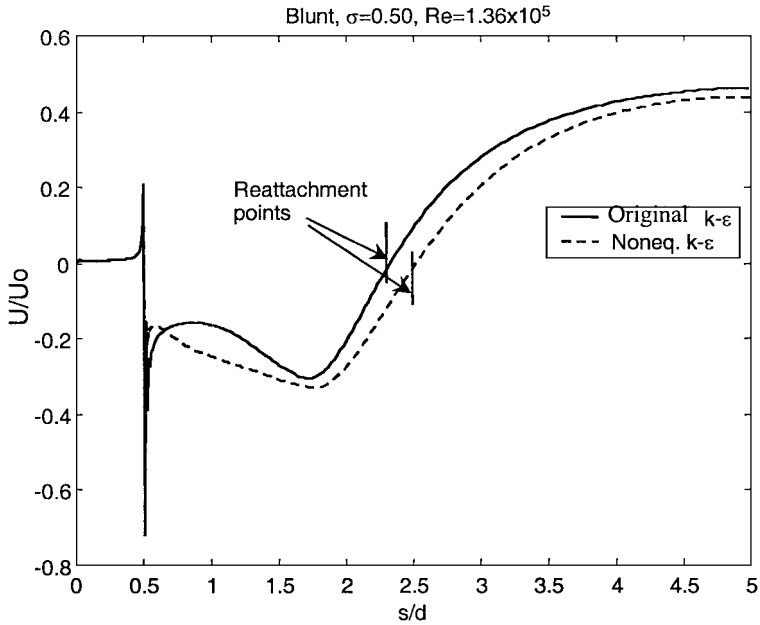

FIG. 11. Comparison of u-velocity along the surface obtained from different turbulence models ($\sigma = 0.50$, $C_{\text{dest}} = 9 \times 10^3$, $C_{\text{prod}} = 6 \times 10^3$, $\rho_l/\rho_v = 1000$).

recirculating zone, as shown in Fig. 11. Although the predictions of pressure are less sensitive to turbulence modeling, other quantities, such as wall shear stress and velocity profiles, can be more affected by it. Due to lack of experimental guidance, we will not present detailed results from the computational study.

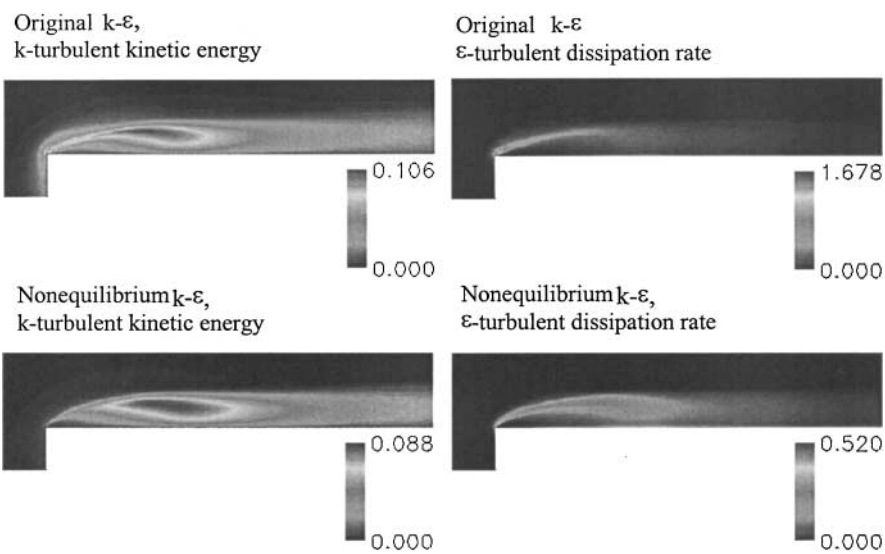

FIG. 12. Comparison of turbulence quantities obtained from different turbulence models ($\sigma = 0.50$, $C_{\text{dest}} = 9 \times 10^3$, $C_{\text{prod}} = 6 \times 10^3$, $\rho_l/\rho_v = 1000$).

5. SUMMARY AND CONCLUSIONS

A pressure-based method for cavitating flow computations is presented and assessed. Single-fluid Navier–Stokes equations, cast in their conservative form, along with a volume fraction transport equation, are employed. The flow is computed in both phases with the vapor pressure recovered inside the cavity via a mass transfer model. A pressure–velocity–density coupling scheme is developed to treat cavitating conditions. While no temperature, and hence no Mach number, effect is considered in the cavitation model, the resulting pressure–correction equation shares common features with that of high-speed flows, exhibiting a convective–diffusive type, instead of only a diffusive type. Specifically, the convective effect in the pressure–correction equation is important as the vapor mass fraction increases in the cavity region; elsewhere, the pressure–correction equation returns to a purely diffusive type.

Furthermore, similar to high-speed cases, upwinded density interpolation in mass flux computations also aids convergence of the cavitating flow computations. Combined with the multiblock and curvilinear grid systems, the present flow solver can handle large density ratios and complex geometries. For the turbulent flows with sheet cavitation, the density profiles indicate a sharp discontinuity at the closure region with a reentrant jet located downstream of it.

Several issues related to grid resolution, convection schemes, and turbulence modeling have been investigated. The reentrant jet in the closure region can be better resolved with grid refinement. The jet becomes stronger as the cavitation number is lowered. Compared to the original k-ε model, the nonequilibrium version of the k-ε model performs better for the same flow conditions. For cavitating flows, although the predictions of pressure are less affected by turbulence modeling, other quantities, such as wall shear stress and velocity profiles, can be more sensitive to it. More investigation of turbulence modeling for bubbly mixtures is needed. While satisfactory agreement between numerical solutions and physical measurements in wall pressure distribution can be maintained with variations in grid resolution and parameters in the cavitation model, other aspects, such as the density distribution, are found to exhibit much higher sensitivity to them. Based on the numerical solutions, physical insight into the vorticity distribution and condensation and evaporation dynamics is gained.

For the cavitation numbers considered, steady-state assumption works well for the hemispherical object, and facilitates reasonable predictions for the blunt object. Unsteady computations are expected to offer improved insight and will be our next focus for future study.

ACKNOWLEDGMENTS

This study has been supported partially by ONR and NSF. The authors thank Robert F. Kunz and Jules W. Lindau for helpful discussions on the cavitation model.

REFERENCES

1. G. K. Batchelor, *An Introduction to Fluid Dynamics* (Cambridge Univ. Press, New York, 1967).
2. R. T. Knapp, J. W. Daily, and F. G. Hammitt, *Cavitation* (McGraw–Hill, New York, 1970).
3. Y. Lecoffre, *Cavitation Bubble Trackers* (Balkema, Brookfield, VT, 1999).

4. Y. Shen and P. Dimotakis, The influence of surface cavitation on hydrodynamic Forces, in *Proceedings 22nd ATTC* (St. Johns, 1989), pp. 44–53.
5. B. Stutz and J. L. Reboud, Two-phase flow structure of sheet cavitation, *Phys. Fluids* **9**(12), 3678 (1997).
6. Y. Chen and S. D. Heister, A numerical treatment for attached cavitation, *J. Fluids Eng.* **116**, 613 (1994).
7. M. Deshpande, J. Feng, and C. L. Merkle, Numerical modeling of the thermodynamic effects of cavitation, *J. Fluids Eng*. **119**, 420 (1997).
8. Y. Delannoy and J. L. Kueny, Cavity flow predictions based on the Euler equations, *ASME Cavitation and Multi-Phase Flow Forum* **109**, 153, (1990).
9. Y. Chen and S. D. Heister, Modeling hydrodynamic nonequilibrium in cavitating flows, *J. Fluids Eng.* **118**, 172, (1996).
10. Y. Ventikos and G. Tzabiras, A numerical method for the simulation of steady and unsteady cavitating flows, *Comput. Fluids* **29**, 63, (2000).
11. J. R. Edwards, R. K. Franklin, and M. S. Liou, Low-diffusion flux-splitting methods for real fluid flows with phase transitions, *AIAA J.* **38**(9), 1624 (2000).
12. A. Kubota, H. Kato, and H. Yamaguchi, A new modelling of cavitating flows: A numerical study of unsteady cavitation on a hydrofoil section, *J. Fluid Mech.* **240**, 59 (1992).
13. L. Rayleigh, On the pressure developed in a liquid during the collapse of a spherical cavity, *Phil. Mag*. **34**, 94 (1917).
14. M. S. Plesset, The dynamics of cavitation bubbles, *Trans. ASME, J. Appl. Mech.* **16**, 228 (1949).
15. A. K. Singhal, N. Vaidya, and A. D. Leonard, Multi-dimensional simulation of cavitating flows using a PDF model for phase change, in *The 1997 ASME Fluids Engineering Division Summer Meeting* (ASME Paper FEDSM97-3272, 1997).
16. C. L. Merkle, J. Feng, and P. E. O. Buelow, Computational modeling of the dynamics of sheet cavitation, in *Proceedings Third International Symposium on Cavitation Grenoble, France 1998*.
17. R. F. Kunz, T. S. Chyczewski, D. A. Boger, D. R. Stinebring, and H. J. Gibeling, Multi-phase CFD analysis of natural and ventilated cavitation about submerged bodies, in *Proceedings Third ASME/JSME Joints Fluids Engineering Conference* (ASME Paper FEDSM99-7364, 1999).
18. R. F. Kunz, D. A. Boger, D. R. Stinebring, T. S. Chyczewski, J. W. Lindau, H. J. Gibeling, S. Venkateswaran, and T. R. Govindan, A preconditioned Navier–Stokes method for two-phase flows with application to cavitation prediction, *Comput. Fluids* **29**, 849 (2000).
19. V. Ahuja, P. A. Cavallo, and A. Hosangadi, Multi-phase flow modeling on adaptive unstructured meshes, in *AIAA Fluids 2000 and Exhibit*, (AIAA-2000-2662, 2000).
20. S. Venkateswaran, J. W. Lindau, R. F. Kunz, and C. L. Merkle, Preconditioning algorithms for the computation of multi-phase mixture flows, in *AIAA 39th Aerospace Sciences Meeting & Exhibit* (AIAA-2001-0125, —.
21. S. V. Patankar, *Numerical Heat Transfer and Fluid Flow* (Hemisphere, Washington DC, 1980).
22. J. P. Vandoormal and G. D. Raithby, Enhancements of the SIMPLE method for predicting incompressible fluid flows, *Numer. Heat Transfer* **7**, 147 (1984).
23. W. Shyy, *Computational Modeling for Fluid Flow and Interfacial Transport* (Elsevier, Amsterdam/ New York, 1994; revised printing 1997).
24. W. Shyy, S. M. Correa, and M. E. Braaten, Computation of flow in a gas turbine combustor, *Combust. Sci. Tech.* **58**, 97 (1988).
25. W. P. Jones and B. E. Launder, The prediction of laminarization with a two-equation model of turbulence, *Int. J. Heat Mass Trans.* **15**, 301 (1972).
26. W. Shyy, S. S. Thakur, H. Ouyang, J. Liu, and E. Blosch, *Computational Techniques for Complex Transport Phenomena* (Cambridge Univ. Press, New York, 1997).
27. S. S. Thakur, J. F. Wright, W. Shyy, and H. Udaykumar, SEAL: *A Computational Fluid Dynamics and Heat Transfer Code for Complex 3-D Geometries* (Univ. Florida, Gainesville 1997).
28. W. Shyy and S. S. Thakur, A controlled variation scheme in a sequential solver for recirculating flows. I. Theory and formulation, *Numer. Heat Transfer B* **25**(3), 245 (1994a).

29. W. Shyy and S. S. Thakur, A controlled variation scheme in a sequential solver for recirculating flows. Part II. Applications, *Numer. Heat Transfer A* **25**(3), 273 (1994b).
30. A. Harten, High resolution schemes for hyperbolic conservation laws, *J. Comput. Phys.* **49**, 357 (1984).
31. W. Shyy and M. E. Braaten, Adaptive grid computation for inviscid compressible flows using a pressure correction method, in *Proceedings AIAA/ASME/SIAM/APS First National Fluid Dynamics Congress* (AIAA-CP 888, 1988).
32. K. C. Karki and S. V. Patankar, Pressure based calculation procedure for viscous flows at all speeds in arbitrary configurations, *AIAA J.* **27**(9), 1167 (1989).
33. J. H. Ferziger and M. Peric, *Computational Methods for Fluid Dynamics*, 2nd ed. (Springer Verlag, Berlin 1999).
34. H. Rouse and J. S. McNown, Cavitation and Pressure Distribution, Head Forms at Zero Angle of Yaw, Studies in Engineering, Bulletin 32 (State University of Iowa, 1948).
35. C. E. Brennen, *Cavitation and Bubble Dynamics* (Oxford Univ. Press, New York, 1995).
36. S. Gopalan and J. Katz, Flow structure and modeling issues in the closure region of attached cavitation, *Phys. Fluids.* **12**(4), 895 (2000).
37. J. Katz, Cavitation phenomena within regions of flow separation, *J. Fluid Mech.* **140**, 397 (1984).
38. D. R. Stinebring, M. L. Billet, J. W. Lindau, and R. F. Kunz, Developed cavitation-cavity dynamics, VKI Lecture Series on Supercavitating Flows (VKI Press, Brussels, 2001).